Genome Biology

METHOD

Open Access

SiCLAT: simultaneous imaging of chromatin loops and active transcription in living cells

Xin Wan[1*], Jie Kong[1], Xiaodi Hu[1], Lulu Liu[2], Yuanping Yang[3], Hu Li[3], Gaoao Liu[1], Xingchen Niu[4,5], Fengling Chen[6], Dan Zhang[4,5], Dahai Zhu[1,3*] and Yong Zhang[1*]

*Correspondence: xinwan@ibms.pumc.edu.cn; dhzhu@pumc.edu.cn; yongzhang@ibms.pumc.edu.cn

[1] State Key Laboratory for Complex, Severe, and Rare Diseases, Institute of Basic Medical Sciences, Chinese Academy of Medical Sciences and School of Basic Medicine, Peking Union Medical College, Beijing, China
[2] Center for Biomedical Technology of National Infrastructures for Translational Medicine, State Key Laboratory of Complex, Severe, and Rare Diseases in Peking Union Medical College Hospital, Beijing, China
[3] Bioland Laboratory (Guangzhou Regenerative Medicine and Health Guangdong Laboratory), Guangzhou, China
[4] Experimental Center, Shandong University of Traditional Chinese Medicine, Jinan, China
[5] Key Laboratory of Traditional Chinese Medicine Classical Theory, Ministry of Education, Shandong University of Traditional Chinese Medicine, Jinan, China
[6] Center for Stem Cell Biology and Regenerative Medicine, MOE Key Laboratory of Bioinformatics, New Cornerstone Science Laboratory, School of Life Sciences, Tsinghua University, Beijing, China

Abstract

We present SiCLAT, which introduces a dCas9-dCas13d cassette into the mouse genome. This model enables the stable expression of both dCas9 and dCas13 proteins in diverse cell populations, facilitating concurrent labeling of DNA and RNA across various cell types. Using SiCLAT, we accurately labeled chromatin loop anchor interactions and associated gene transcription during myogenic differentiation. This imaging system offers a novel means of directly observing cis-element interactions and the corresponding gene transcription in living primary cells, thus providing real-time imaging for comprehensive mechanistic investigations of dynamic enhancer-promoter or enhancer-enhancer interactions in regulating transcription activation within living cells.

Keywords: CRISPR imaging, Non-repetitive DNA and RNA imaging, Genetic mouse model, Living primary cell, 3D genome, Enhancer and promoter interaction

Introduction

In eukaryotes, the three-dimensional (3D) organization of chromatin within the nucleus critically regulates gene expression during development, underscoring the vital connection between spatial structure and functional outcomes. Over the past decade, advancements in Hi-C and its derivative techniques have facilitated the generation of comprehensive datasets of chromatin interactions. These datasets are instrumental in deciphering complex, high-dimensional chromatin architectures, including nuclear compartments, topologically associated domains (TADs), and chromatin loops [1, 2]. To further resolve these structures and elucidate their functions in single cells, chromatin tracing techniques has been developed, including ORCA [3], MERFISH [4], MINA [5], and Hi-M [6, 7], which are capable of concurrently profiling chromosome architecture and transcriptional activity within individual cell nuclei. Such approaches offer the insights into the intricate structure at a finer scale, including specific topologically associated domains (TADs), sub-TADs, and chromatin loops. Importantly, the genome structure is dynamic, particularly with respect to the function of enhancer-promoter

(E-P) interactions [8, 9] in controlling the transcription of lineage-specific genes during development [10–15]. The exploration of the dynamic genome structure has prompted the development of live-cell imaging techniques in various biological systems such as in Drosophila [8] and mouse embryonic stem cells (ESCs) [9], facilitating our understanding of the dynamic interplaying between E-P and transcriptional activity at the single-cell level.

It is worth to know that the cis-elements or other chromatin loop anchors rarely contain repetitive DNA sequences; therefore, researchers have endeavored to label non-repetitive genomic loci in living cells by introducing extraneous repetitive sequences [8, 9, 15–17] or using modified long-sequence gRNAs [18–20] to amplify fluorescence signals. However, those imaging tools are still scarce to label chromatin loop anchors with their corresponding transcripts in different primary cells to explore their structure dynamics and transcriptional regulation of gene expression.

To address these, we herein present a rational design for assembling fluorescent ribonucleoproteins (fRNPs) within the nuclei of living cells. We developed a multifunctional transgenic mouse model (referred to as SiCLAT) by integrating a CAG promoter-LSL-dCas9-P2A-dCas13d-PolyA cassette into the mouse genome. This strategic design enabled us to stably express dCas9 and dCas13 proteins across diverse cell populations by either crossing SiCLAT mice with mice harboring Cre under cell-type-specific promoters or transducing primary cells with Cre-expressing adenovirus. The fRNPs assembled in the nuclei of living cells facilitated the concurrent labeling of chromatin loop anchors (DNA) and their associated gene transcription (nascent RNA) across various cell types. Using the SiCLAT imaging system, we examined the ability of simultaneous labeling chromatin loop anchors and associated gene transcription during myogenic differentiation. Our data indicate that SiCLAT could potentially serve as a convenient and viable imaging system to provide reliable data for the future functional and dynamic understanding of chromatin structure in living cells.

Results

Rational design of SiCLAT for co-imaging of DNA and RNA in living cells

To visualize E-P chromatin loops and their associated gene transcription during cell lineage differentiation, we developed a multifunctional mouse model for imaging chromatin loops and transcription (SiCLAT). We first introduced a CAG-LSL-dCas9-P2A-dCas13d-PolyA cassette into the mouse genome to generate a random transgenic mouse model (Fig. 1); this enabled us to stably express dCas9 and dCas13 proteins within various cell populations by crossing the mice expressing cell lineage-specific Cre or directly delivering plasmids/viruses encoding Cre recombinase into primary cells obtained from these mice. The delivery of fluorescent guide RNAs (fgRNAs) via electroporation promotes the fgRNAs binding with dCas9 and dCas13d to assemble the fRNP in the primary cell nucleus, which lights the prospective loci by fRNP targeting and allows us to simultaneously label chromatin loop anchors (DNA) and gene transcription (RNA) across diverse cell types (Fig. 1).

Before generating the engineered SiCLAT mice, we first tested whether nuclear-localized dCas9 proteins expressed in cells would undergo efficient assembly with electroporation-delivered fgRNAs to generate the fluorescent ribonucleoproteins

(fRNPs) needed for genomic DNA imaging. To this end, we transfected primary fibroblast with a dCas9-EGFP plasmid to pre-express the dCas9 protein, and then electroporated the cells with fgRNA-Cy5 designed to target the A-kinase anchor protein locus (*Akap6*), which contains an 87-copy repetitive sequence [21] (Additional file 1: Fig. S1a). Imaging revealed that the *Akap6* locus could be effectively visualized using either dCas9-EGFP or fgRNA-Cy5 (Additional file 1: Fig. S1b), with fgRNA-Cy5 imaging exhibiting a stronger signal intensity and higher signal-to-background (S/B) ratio compared to dCas9-EGFP visualization (Additional file 1: Fig. S1b-d). This was consistent with a previous report indicating that fgRNA-mediated imaging is superior to fluorescent-dCas9 DNA labeling [22]. Our results further revealed that dCas9-fRNP was effectively assembled in the nucleus for genomic DNA imaging. Meanwhile, recent work highlighted the successful application of dCas13d-fRNP for cellular RNA imaging [22]. Collectively, the present and previous results provide support for our rational design of the SiCLAT imaging model to enable the simultaneous labeling of DNA and RNA in living cells.

To validate the functionality of the engineered SiCLAT system, mouse-derived primary cells were infected with adenovirus expressing the Cre recombinase (Ad-Cre-EGFP) to activate dCas9 expression, and electroporation was used to deliver fgRNA-Cy5 targeting the *Akap6* locus (Additional file 1: Fig. S2a). fgRNA-Cy5 targeting Galectin 4 (*Gal4*) was used as a negative control, as previously reported [23]. We successfully detected the Cy5 signal at the *Akap6* locus, whereas no signal was detected for *Gal4* (Additional file 1: Fig. S2b). Remarkably, one or both alleles of *Akap6* were lighted in cells that were Cre-positive (Cre^+) and EGFP-positive ($EGFP^+$), but not in those that were Cre-negative (Cre^-) and EGFP-negative ($EGFP^-$), indicating the high-level specificity of the SiCLAT DNA imaging system (Additional file 1: Fig. S2c-e). Significantly, SiCLAT DNA imaging demonstrated consistent efficacy across a diverse array of tested cell types, including but not limited to renal cells, hepatocytes, neural stem cells, myoblasts, preadipocytes, and fibroblasts (Additional file 1: Fig. S2f).

We compared the DNA imaging ability of SiCLAT with that of the recently developed LiveFISH [22] technique and found that SiCLAT and LiveFISH demonstrated comparable S/B ratios and sensitivity levels for allele pair visualization (Additional file 1: Fig. S1e-g). These findings compellingly suggest that SiCLAT is a viable DNA imaging system that can label DNA via endogenous dCas9-driven assembly of nuclear fRNPs.

(See figure on next page.)

Fig. 1 Schematic of SiCLAT. **a** SiCLAT mice were generated by introducing a CAG-LSL-dCas9-P2A-dCas13d-PolyA cassette into the mouse genome (CAG, CMV early enhancer/chicken beta actin promoter; LSL, LoxP-Stop-LoxP; P2A, porcine teschovirus-1 2A). The stable co-expression of dCas9 and dCas13 within various cell populations was achieved by crossing SiCLAT mice with cell lineage-specific Cre mice or by directly delivering plasmids/viruses encoding Cre recombinase into primary cells obtained from the SiCLAT mice. Simultaneous labeling of DNA and RNA across diverse cell types was accomplished by delivering fluorescent guide RNAs (fgRNAs) via electroporation. **b** To visualize chromatin loops and their associated gene transcription, loop anchors found generally within non-repetitive DNA regions were labeled with pools of 15 fgRNAs and nascent RNA transcripts were labeled with pools of 20 fgRNAs, respectively

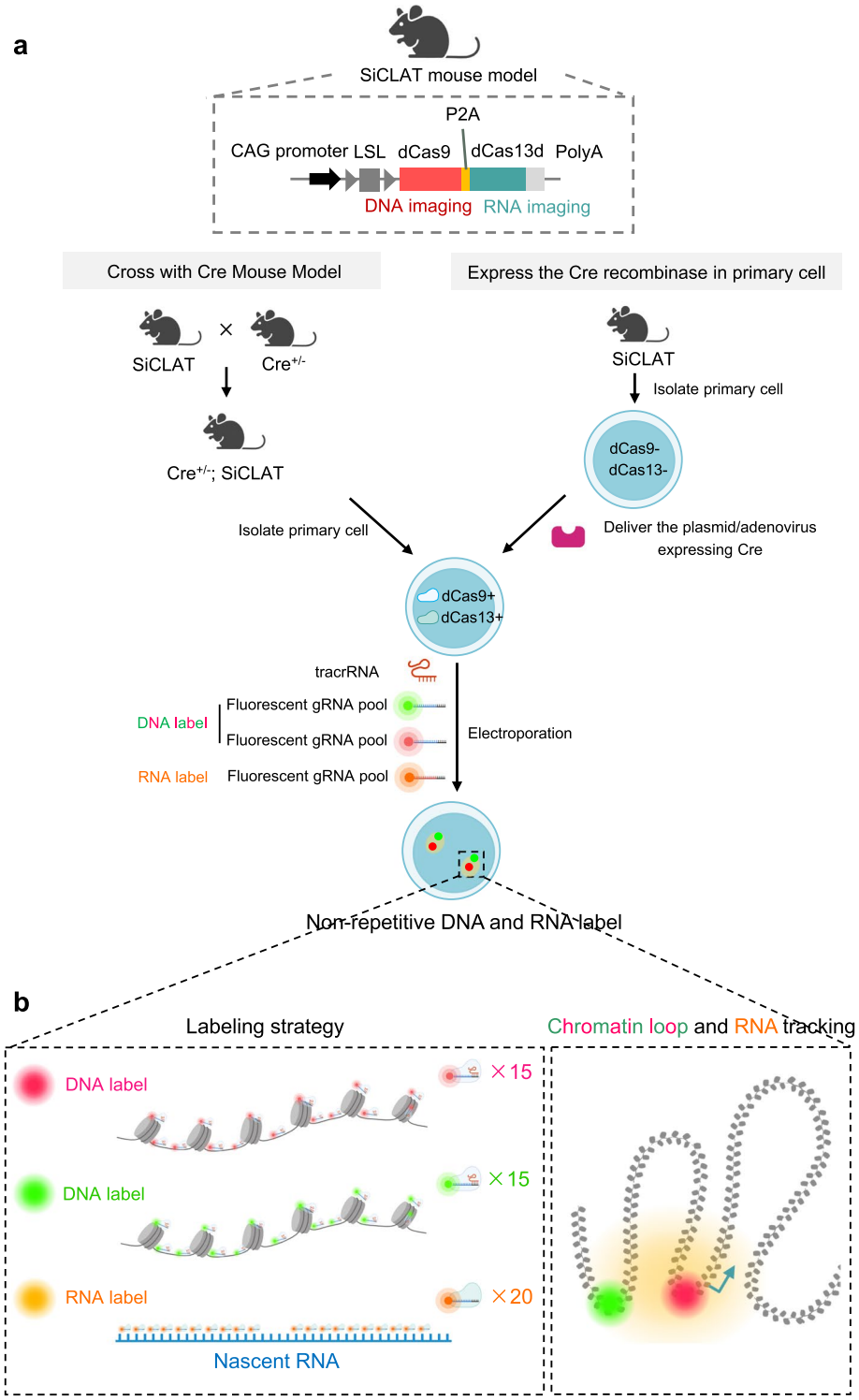

Fig. 1 (See legend on previous page.)

SiCLAT enables visualization of non-repetitive DNA in living cells

Next, we examined the ability of the SiCLAT to visualize non-repetitive genomic DNA by delivering multiple fgRNAs. To accomplish this, we first designed experiments to ascertain how many fgRNAs should be in a fgRNA pool to label non-repetitive DNA with high specificity and sensitivity. We designed separate fgRNAs for three loci on chromosome 12 that have different numbers of repeats (*Akap6*, 87 copies; *Sμ*, 18 copies; *Sγ1*, 7 copies) [21] (Additional file 1: Fig. S3a) and individually tested their labeling efficiency. One or two alleles were detected in living cells for all three loci (Additional file 1: Fig. S3b-d). The efficiency of paired-allele labeling was lower for *Sμ* (18 copies) than for *Akap6* (87 copies), whereas their single-allele labeling was similar Additional file 1: Fig. S3b, d). This suggests that ~ 18 targeted locations (repeats) are adequate for non-repetitive DNA labeling within living cells.

Based on these findings, we used a pool of 15 fgRNAs to assess the capacity of SiCLAT to enable visualization of non-repetitive genomic DNA. We selected five individual non-repetitive genomic loci known to be present within enhancer-promoter (E-P) chromatin loop anchors in muscle cells [24]: the *Myogenin* gene promoter (*Myog*) and the myosin-binding protein H gene promoter (*Mybph*) on chromosome 1 and the actin alpha cardiac muscle 1 gene promoter (*Actc1-P*) and its enhancers (*Actc1-E1*, *Actc1-E3*) on chromosome 2 (Additional file 1: Fig. S4a, b). For each locus, we designed 15 fgRNAs tiling regions of 1 ~ 3 kb and end-labeled each set with an individual fluorophore (Atto647N, Atto488, FAM, TAMRA, Cy5). SiCLAT mice were crossed with *Pax7*-Cre mice to specifically activate dCas9 expression in myoblasts (Additional file 1: Fig. S5a), and fibroblasts isolated from SiCLAT mice were infected with Cre recombinase-expressing adenovirus to activate the expression of dCas9. The fgRNA pool for each locus was electroporated into the primary fibroblasts, myoblasts, and differentiated myocytes and subjected to DNA imaging. We found that all five non-repetitive genomic loci were labeled for single or paired alleles, with relatively high S/B ratios obtained after deconvolution processing in the three cell types (Fig. 2a,b and Additional file 1: Fig. S5b-g). Moreover, the fgRNA pool targeting the genomic region near the gene did not significantly affect

(See figure on next page.)

Fig. 2 SiCLAT enables visualization of non-repetitive DNA in living cells. **a** Representative images showing visualization of five non-repetitive genomic loci in primary myoblasts isolated from *Pax7*-Cre; SiCLAT- or SiCLAT-derived primary fibroblasts infected with Ad-Cre (*Gene*-fluo: *Myog*-Atto647, *Mybph*-Atto488, *Actc1(P)*-FAM, *Actc1(E1)*-TAMRA, *Actc1(E3)*-Cy5). Scale bar, 2 μm. **b** Fractions of cells with single- or paired-allele labeling of the five non-repetitive genomic loci in primary myoblasts isolated from *Pax7*-Cre; SiCLAT mice. **c** Experimental design for co-labeling of two sites (*Myog* and *Mybph*) or three sites (*Actc1-P*, *Actc1-E1*, *Actc1-E3*) of non-repetitive genomic loci in *Pax7*-Cre; SiCLAT mouse-derived primary myoblasts, primary myocytes or SiCLAT-derived fibroblasts infected with Ad-Cre. **d** Representative images showing co-labeling of *Myog* (red) and *Mybph* (green) or co-labeling of *Actc1* E3 (Violet), *Actc1* P (cyan), and *Actc1* E1 (yellow) in primary fibroblasts, primary myoblasts, or myocytes, as described in panel **c**. Scale bar, 2 μm. **e** Representative images showing co-labeling of *Myog* (red) and *Mybph* (green) in *Pax7*-Cre; SiCLAT mouse-derived primary myoblasts cultured for 24 h and 72 h. Scale bar, 3 μm (left), 0.5 μm (right). **f** Fractions of cells with two-site co-labeling (*Myog* and *Mybph*) or single-site labeling (either *Myog* or *Mybph*) from among the primary myoblasts presented in panel **e**. **g** Representative images of the *Myog* or *Actc1* E3 locus with Tn5-FISH followed by SiCLAT labeling in fibroblasts. The images show the signal of the *Myog* locus (green, Tn5-FISH signal; red, SiCLAT signal) in the nucleus labeled with a white arrow in the original image. Scale bars, 5 μm. **h**, **i** Percentage of yellow signal (the merged signal with Tn5-FISH and SiCLAT)/red signal (SiCLAT) in the living cells

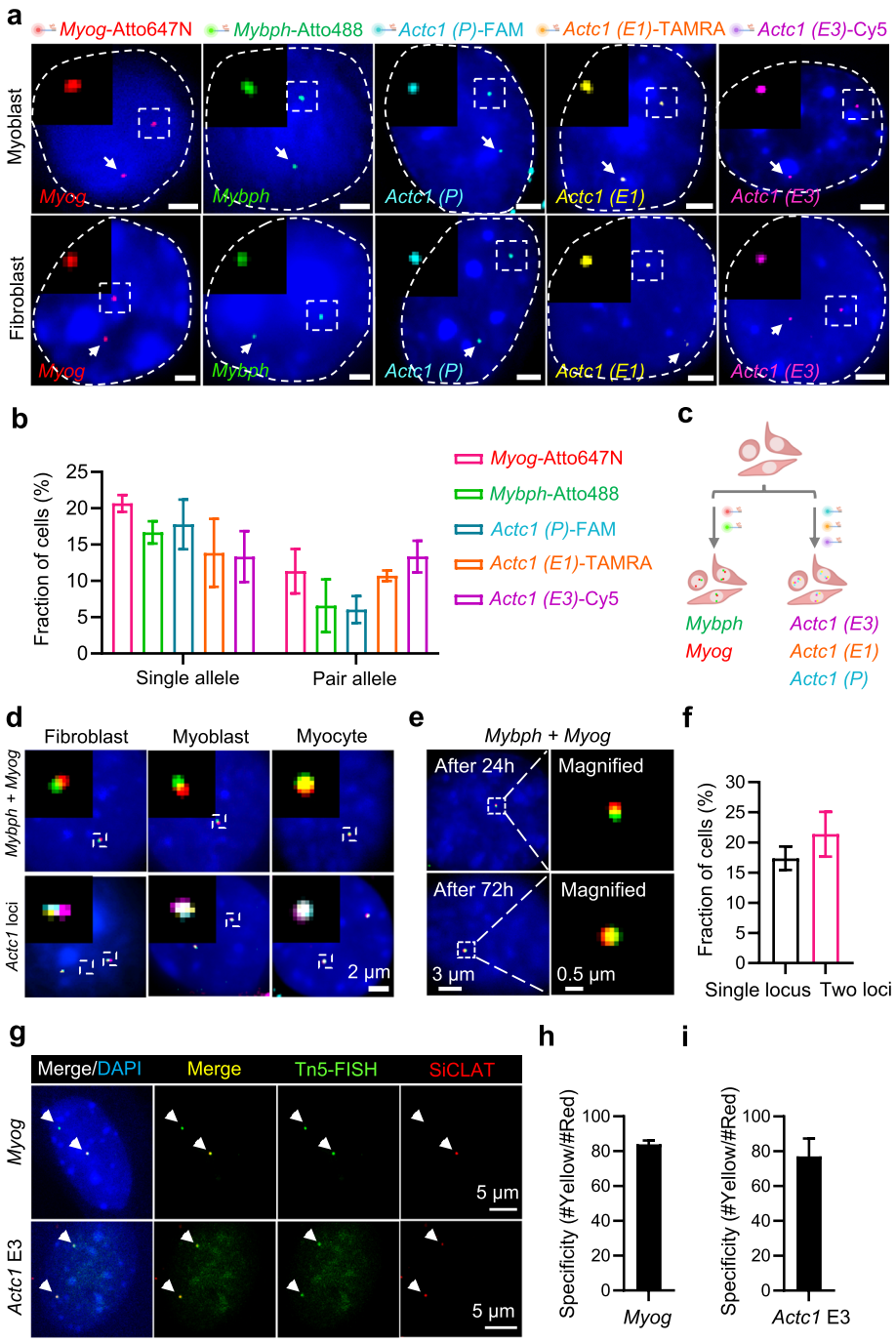

Fig. 2 (See legend on previous page.)

gene transcription (Additional file 1: Fig. S5h, i). These results underscore the capacity of SiCLAT to label non-repetitive DNA within living cells.

To extend the application of SiCLAT, we used it to simultaneously label two or three genomic loci within non-repetitive sequences in living cells (Fig. 2c, Additional file 1: Fig. S4c, d, S5j, k, Additional file 2: Video S1 and Additional file 3: Video S2). The results showed that SiCLAT enabled the successful co-imaging of *Myog*/*Mybph* or *Actc1-P/*

Actc1-E1/*Actc1-E3* across the three cell types (Fig. 2d, Additional file 1: Fig. S5l, m, Additional file 4: Video S3 and Additional file 5: Video S4). Importantly, the SiCLAT-based labeling of non-repetitive DNA remained stable in living cells at 24 and 72 h (Fig. 2e, f). These results collectively indicate that SiCLAT represents a viable system for long-term labeling of non-repetitive DNA in living cells.

To examine labeling specificity of SiCLAT, we conducted Tn5-FISH followed by SiCLAT labeling at both the *Myog* locus and the *Actc1* E3 locus (Fig. 2g). We demonstrated that more than 80% of *Myog* signals labeled with SiCLAT were overlapped with the signals labeled by Tn5-FISH (Fig. 2h), more than 75% of *Actc1* E3 signals were merged each other labeled by SiCLAT and Tn5-FISH (Fig. 2i), indicating the specificity of the SiCLAT imaging. Together, our SiCLAT imaging system has a great potential to achieve higher specificity and reliability for visualization of non-repetitive DNA in living cells.

SiCLAT-based non-repetitive DNA labeling enables lighting up chromatin loop anchors

We then tested the potential of SiCLAT imaging for directly observing E-P chromatin loop formation in living cells. Based on our BL-Hi-C data [24], two E-P interactions that are 385 kb and 580 kb respectively were selected to visualize the E-P loops with the SiCLAT system (Fig. 3a, d, Additional file 1: S6a, b). As these two E-P interactions were specifically formed in the differentiated myocytes but not observed in the undifferentiated myoblasts and fibroblasts (Fig. 3a, d, Additional file 1: S6a, b), the imaging data obtained from the undifferentiated myoblasts and fibroblasts would be served as nice negative controls to demonstrate E-P loop formation in the differentiated myocytes. To this end, the SiCLAT-derived primary myoblasts or fibroblasts were infected with Cre recombinase-expressing adenovirus (Ad-Cre) to activate the expression of dCas9 (Additional file 1: Fig. S6c). Fifteen fgRNAs designed for each anchor (Additional file 8: Table S2) were electroporated into the primary myoblasts, differentiated myocytes and fibroblasts, then subjected to DNA imaging (Additional file 1: Fig. S6c). We did observe the two E-P loops formed in the differentiated muscle cells, as evidenced by the overlapped fluorescent spots of enhancer (red) and promoter (green) in the muscle cells (Fig. 3b, c and e, f). However, in undifferentiated myoblasts and fibroblasts, the signals of enhancer (red) and promoter (green) were clearly separated in two distinct spots, indicating that neither E-P interactions occurred in either non-muscle cells or undifferentiated muscle cells (Fig. 3b, c and e, f and Additional file 1: Fig. S6d). Together, our data indicate that SiCLAT-based non-repetitive DNA labeling enables visualizing E-P chromatin loops.

It has been reported that some of E-P chromatin loops are shorter than 200 kb [25, 26], we next examined the capability of the SiCLAT to visualize these shorter chromatin loops. We recently reported that there is a chromatin interaction between the *Myog* promoter and the *Mybph* promoter (P-P interaction) [24]. This chromatin loop (~100 kb) specifically forms in differentiated myocytes (Fig. 3g, h) and is functionally required for the transcriptional regulation of *Myog* and *Mybph* during differentiation (Additional file 1: Fig. S4e, f). Thus, we tested the ability of SiCLAT to light up *Myog-Mybph* loop anchors during muscle cell differentiation and a negative control (NC) locus which has an equivalent genomic separation (at the 100 kb downstream of *Mybph*) but do

not interact with *Mybph* was selected to validate the imaging specificity of the SiCLAT (Fig. 3g). The confocal microscopy imaging showed that the *Myog-Mybph l*oop was only formed in the differentiated myocytes, as evidenced by shorter 3D distance in myocytes compared to the myoblasts (Fig. 3i, j). However, the 3D distance between *NC* and *Mybph* was significantly greater than that of *Myog-Mybph* loci in the myocytes (Fig. 3i, j), which is consistent with the BL-Hi-C data that there is no interaction between *NC* and *Mybph* (Fig. 3g). We also performed the super-resolution imaging of *Myog-Mybph* loop. Consistent with our confocal microscopy data, Multi-SIM imaging also showed the anchors with two distinct fluorescent spots in the undifferentiated muscle cells (Additional file 1: Fig. S7), demonstrating the imaging resolution in our SiCLAT system could be adequate to provide reliable observation to fluorescent spots in genomic distance < 100 kb.

We further corroborate the accurateness of the SiCLAT imaging by using a genetic perturbation system. Our previous work has demonstrated that the *Myog-Mybph* chromatin loop formation during muscle cell differentiation is mediated by the muscle lineage-specific transcription factor MyoD [24]. Knockout of *MyoD* significantly reduced *Myog-Mybph* interactions [24]. Therefore, *MyoD* knockout mice provide a genetic

(See figure on next page.)

Fig. 3 SiCLAT-based non-repetitive DNA labeling enables lighting up chromatin loop anchors. **a** BL-Hi-C map showing the representative E-P interactions (385 kb) in the undifferentiated and differentiated muscle cells. Black arrowheads showing the chromatin loops which are reduced in undifferentiated muscle cells compared with the differentiated muscle cells. The BL-Hi-C data of muscle cells are from our previous work [24]. **b** Representative images of E-P (385 kb) in nuclei of undifferentiated and differentiated muscle cells, respectively, visualized with the SiCLAT. The zoom-in images showed the magnified signals in the nucleus labeled with a white arrow in the original image. Scale bars, 2 μm. **c** Boxplot of the 3D distance of the EP (385 kb) in undifferentiated and differentiated muscle cells. Data are presented as mean ± SD. *p*-values were determined using unpaired two-tailed Student's *t*-test, $p < 0.0001$. **d** BL-Hi-C map showing the representative E-P interactions (580 kb) in the undifferentiated and differentiated muscle cells. Black arrows showing the chromatin loops which are reduced in undifferentiated muscle cells compared with the differentiated muscle cells. The BL-Hi-C data of muscle cells are from our previous work [24]. **e** Representative images of E-P (580 kb) in nuclei of undifferentiated and differentiated muscle cells, respectively, visualized with the SiCLAT. The zoom-in images showed the magnified signals in the nucleus labeled with a white arrow in the original image. Scale bars, 2 μm. **f** Boxplot of the 3D distance of the EP (580 kb) in undifferentiated and differentiated muscle cells. Data are presented as mean ± SD. *p*-values were determined using unpaired two-tailed Student's *t*-test, $p < 0.0001$. **g** BL-Hi-C map showing the *Myog-Mybph* loop labeled with the black square and equal distance locus labeled with the blue square. The differentiated muscle cell (Myocyte) was shown at the bottom left and undifferentiated muscle cells (Myoblast) was shown at the top right [24]. Schematic illustration of the genomic distance in the *Myog*, *Mybph* and negative control (NC) with equal distance loci shown below. **h** Schematic illustration showing the formation of the chromatin loop presented in **g** during muscle cell differentiation. **i** Representative images showing visualization of the *Myog-Mybph* chromatin loop and *Mybph-NC* sites (red, *Myog* or NC; green, *Mybph*) in the myoblast, myocytes or equal distance. Scale bar, 2 μm. **j** Boxplot showing 3D distance of *Myog-Mybph* chromatin loop or *Mybph-NC* sites in the myoblast and myocyte presented in **i**. Data are presented as mean ± SD. *p*-values were determined using unpaired two-tailed Student's *t*-test, $p < 0.0001$. **k** Schematic illustration showing isolation of primary myoblasts from SiCLAT (WT) or SiCLAT; $MyoD^{flox/flox}$ (SiCLAT-*MyoD*-KO), infected with Ad-Cre to delete *MyoD* and activate dCas9 expression, then induced for differentiation. **l** BL-Hi-C map showing the *Myog-Mybph* loop in the WT and *MyoD* KO muscle cells. Black square showing the chromatin loops which are reduced in *MyoD* KO muscle cells compared with the WT muscle cells. The WT differentiated muscle cells was shown at the bottom left and *MyoD* KO muscle cells was shown at the top right. The BL-Hi-C data of muscle cells are from our previous work [24]. **m** Schematic illustration showing the formation of the chromatin loop presented in **l**. **n** Representative images showing visualization of the *Myog-Mybph* chromatin loop (red, *Myog*; green, *Mybph*) in the WT and *MyoD* KO. Scale bar, 2 μm. **o** Boxplot showing 3D distance in **n**. Data are presented as mean ± SD. *p*-values were determined using unpaired two-tailed Student's *t*-test, $p < 0.0001$. **p** Representative 3D distances of the *Mybph-Myog* chromatin loop in myoblasts and myocytes labeled for 760 s. **q** Representative fluorescent spot in the 3D imaging at the 40 s and 600 s time points in **p**

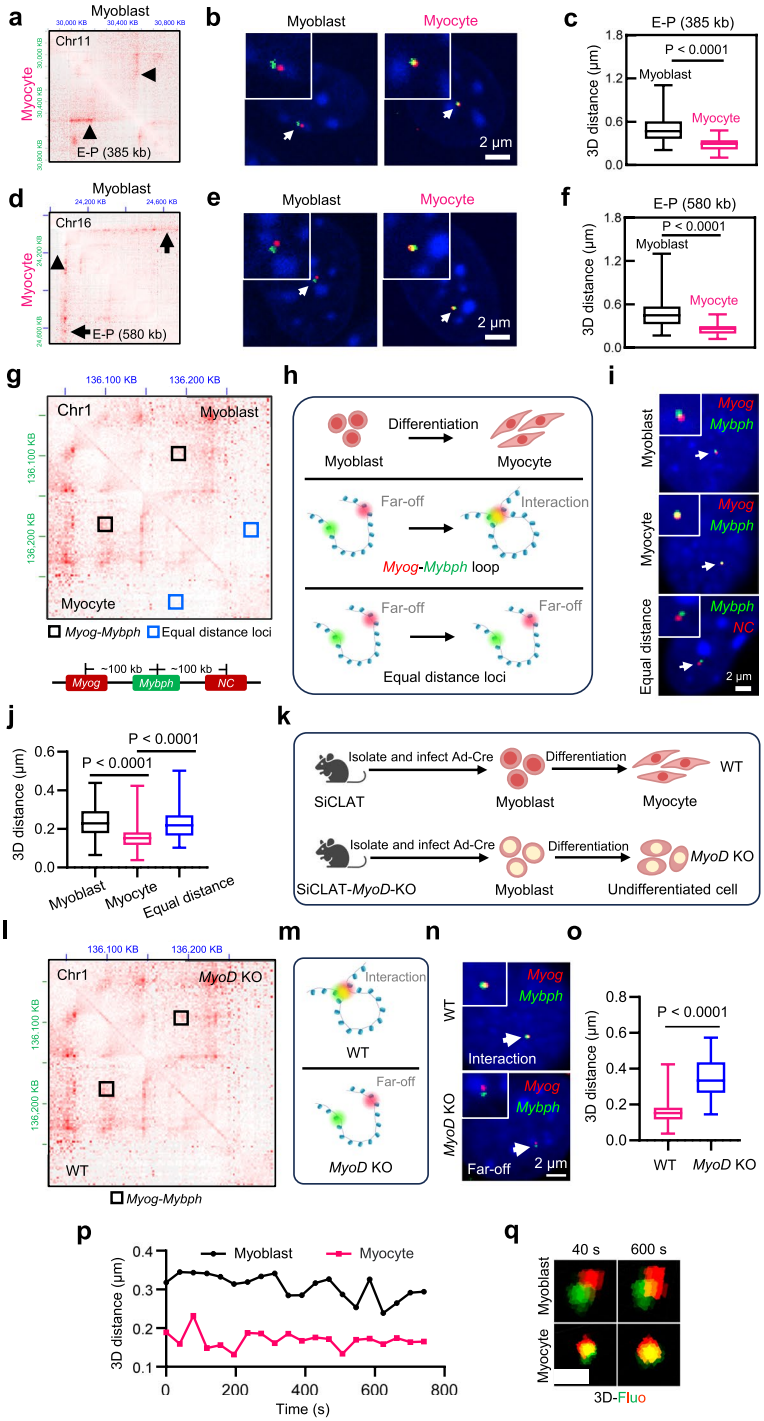

Fig. 3 (See legend on previous page.)

perturbation system to further substantiate *Myog-Mybph* loop formation observed by the SiCLAT imaging data in muscle cells. To this end, we first generated SiCLAT; *MyoD*$^{flox/flox}$ mice (SiCLAT-*MyoD*-KO) to delete MyoD in SiCLAT mice by crossing the *MyoD*$^{flox/flox}$ mice with SiCLAT mice (Fig. 3k and Additional file 1: Fig. S8). The imaging data demonstrated that knockout of *MyoD* disrupted the *Myog-Mybph* chromatin loop

formation, as evidenced by the increased 3D distance between *Myog* and *Mybph* locus, which was consistent with BL-Hi-C data from *MyoD* KO mice (Fig. 3l–o). Together, the genetic perturbation data provided further support that SiCLAT is a powerful DNA imaging tool for visualizing E-P interactions even with relatively short genomic distance (~100 kb).

Next, we examined the capability of SiCLAT for labeling chromatin interactions in several frames in living cells. For the *Myog-Mybph* interaction, the clear and distinct fluorescence signals for both anchors at each time point for 30 min at 3-min intervals was captured in the primary myoblast (Additional file 1: Fig. S9), suggesting that SiCLAT could be used to light up the chromatin loop in a period of time. We further performed live-cell imaging of *Myog-Mybph* loop anchors before (myoblasts) and after (myocytes) the induction of differentiation using different interval times (30 s, 3 min, 12 min) and durations (10 min, 30 min, 120 min). To assist in the visualization of real-time chromatin loop formation, the 3D distances between loop anchors were calculated via spot function with 3D Gaussian fitting using Imaris, a professional image software (Additional file 1: Fig. S10). We found that the *Myog-Mybph* loop anchors were closer in myocytes than in myoblasts, as showed by the 3D distance measurements in individual cells and the averaged distances; this finding aligned with the BL-Hi-C data (Fig. 3g, p, q and Additional file 1: Fig. S11). We also analyzed imaging data obtained for the *Myog-Mybph* loop in fibroblasts and compared it with those from myoblasts and myocytes. The 3D distance was significantly greater in fibroblasts than in myocytes, further supporting the notion that the *Myog-Mybph* loop represents a lineage-specific chromatin structure in myocytes (Additional file 1: Fig. S12 and Additional file 6: Video S5). Taken together, these data support the capability and efficiency of the SiCLAT as a powerful DNA imaging tool for labeling chromatin loops in living cells.

SiCLAT enables visualization of E-P and E-E interaction in living cells

We previously identified a multi-locus interaction in the *Actc1* gene locus [24] that offered an appropriate model for assessing the ability of SiCLAT to label multiple cis-element interactions. The loci, which comprise one promoter and three enhancers, form specifically in myocytes to activate *Actc1* transcription in response to differentiation (Fig. 4a and Additional file 1: Fig. S4g). In addition, our previous work has demonstrated

(See figure on next page.)

Fig. 4 SiCLAT enables visualization of E-P and E-E interaction in living cells. **a** BL-Hi-C map showing the *Actc1* loci consisted of the 3 enhancers labeled with the yellow line segment and the *Actc1* promoter labeled with the red line segment in the differentiated muscle cell at the bottom left or undifferentiated muscle cells at the top right. Resolution, 1 kb. **b** Representative images of the *Actc1* multi-locus interaction labeled with the SiCLAT system in differentiated muscle cells of SiCLAT and SiCLAT-*MyoD*-KO. The zoom-in images show the partial signal of the *Actc1* multi-locus (violet, *Actc1 enhancer 3*; cyan, *Actc1* promoter; yellow, *Actc1 enhancer 1*) in the nucleus labeled with a white box in the original image. Scale bars, 2 μm. Schematic illustration showing the loop formation in the myocyte (left) from the fluorescence image. **c** Boxplot of the 3D distance of the *Actc1* multi-locus in the myoblast, myocyte from SiCLAT and myocyte from SiCLAT-*MyoD*-KO. Data are presented as mean ± SD. *p*-values were determined using unpaired two-tailed Student's *t*-test. **d** Representative 3D distances of the *Actc1* multi-locus labeled for 30 min in a myocyte. **e** Representative 3D fluorescent surface picture of the trajectory over time described in panel **d**, labeled with T2-T11. **f** Representative 3D distances of the *Actc1* multi-locus labeled for 350 s in a myocyte. **g** Representative 3D fluorescent surface picture for the trajectory over time presented in panel **f**, labeled with T1-T4 and T5-T8

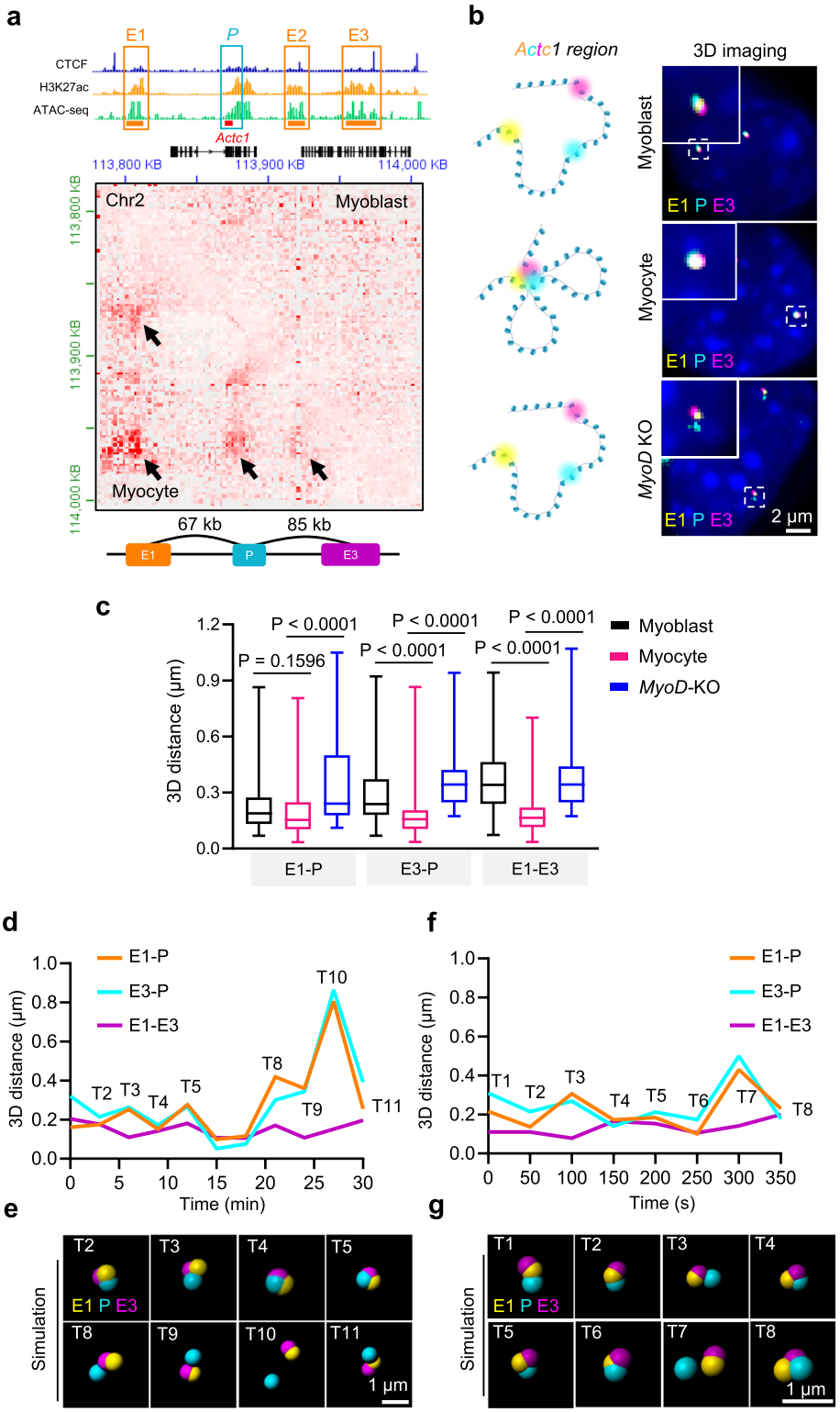

Fig. 4 (See legend on previous page.)

that knockout of *MyoD* significantly reduced the *Actc1* multi-locus interactions [27]. We thus used SiCLAT to perform tri-locus labeling of the *Actc1* promoter (P), enhancer 1 (E1), and enhancer 3 (E3) in myoblasts (SiCLAT), myocytes (SiCLAT), and myocyte (SiCLAT-*MyoD*-KO). The fluorescence snapshots and averaged 3D distance measurements consistently revealed that myocytes had a tighter interaction, which agreed with BL-Hi-C data from these cell types (Fig. 4a–c and Additional file 1: Fig. S13a-c). As a negative control, we conducted imaging in fibroblasts. The 3D distance was consistently higher in fibroblasts than in myocytes, which demonstrates that the formation of the *Actc1* multi-locus interaction is lineage-specific (Additional file 1: Fig. S13d) and was consistent with Hi-C heatmap in other non-muscle cells (Additional file 1: Fig. S13e).

We further examined the *Actc1* multi-locus interaction in living myocytes using intervals of 3 min or 50 s and capturing data over durations of 30 min or 350 s. Our live-cell imaging data show that E-E interaction contained the longest linear genomic distance in this loci shown a very close distance in living cell labeling data, which indicated that SiCLAT enables labeling tri-locus with multi-frame (Fig. 4d–g).

Together, these data support the SiCLAT has the potential to label multi-locus interaction and explore the dynamics of different chromatin loops.

SiCLAT enables co-imaging of non-repetitive DNA and RNA in living cells

A significant strength of the SiCLAT system lies in its potential to in situ labeling endogenous gene transcription. As previously mentioned and shown in Fig. 1, the co-expression of dCas13d plus dCas9 within the cells of SiCLAT mice allows for DNA and RNA to be simultaneously co-imaged within the same living cells. To explore this capability, we first targeted the first intron of *Akap6* (harboring an 87-copy repeat) and examined the ability of our system to co-label repetitive DNA and RNA (Additional file 1: Fig. S14a). A single fgRNA with the 5′ fluorescent dye, FAM, was designed based on the repetitive sequence of the *Akap6* nascent transcript (Additional file 1: Fig. S14a). fgRNA-FAM targeting *Akap6* nascent RNA and fgRNA-Cy5 targeting *Akap6* DNA were co-electroporated into primary myoblasts isolated from *Pax7-Cre*; SiCLAT mice (Fig. 5a). The DNA signals had high S/B ratios in myoblasts and differentiated myocytes, whereas the *Akap6* RNA signal was exclusively detected in differentiated myocytes (Fig. 5b,c and Additional file 1: Fig. S14b-e). The latter finding is consistent with the RNA-seq-based expression pattern previously reported for the *Akap6* mRNA [24]. We also observed a continuous increase of the RNA signal in myocytes during differentiation (Additional file 1: Fig. S14f, g and Additional file 7: Video S6). These findings show that SiCLAT can enable the co-imaging of repetitive DNA and RNA within living cells.

We further tested the ability of SiCLAT to enable co-labeling of non-repetitive DNA and RNA by targeting the *Myog* locus. To achieve this, we designed a pool of 20 *Myog* RNA transcript-targeting fgRNAs bearing the 5′ fluorescent dye, TAMRA (Additional file 1: Fig. S15a). The fgRNA-TAMRA pool targeting the *Myog* RNA and the fgRNA-Atto647N pool targeting the *Myog* gene promoter were co-electroporated into primary myoblasts isolated from *Pax7-Cre*; SiCLAT mice (Fig. 5d). The *Myog* DNA signal had high S/B ratios in both myoblasts and differentiated myocytes, whereas the *Myog* RNA signal was significantly stronger in differentiated myocytes than in myoblasts (Fig. 5e, f, Additional file 1: Fig. S4e). The latter finding is consistent with the

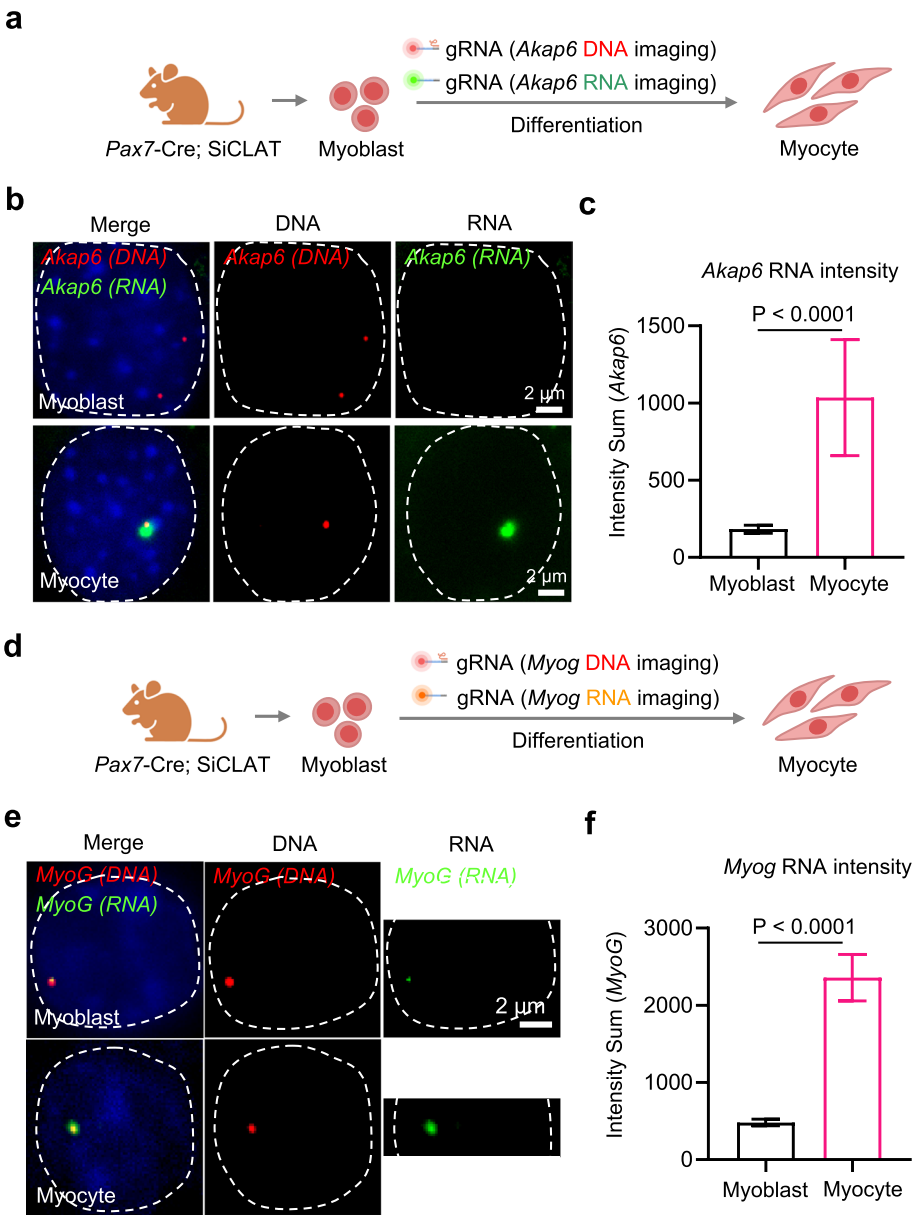

Fig. 5 SiCLAT enables co-imaging of non-repetitive DNA and RNA in living cells. **a** Schematic showing the experimental design for visualizing the *Akap6* DNA and RNA in primary myoblasts isolated from *Pax7*-Cre; SiCLAT mice and induced to undergo differentiation. **b** Representative images showing the visualization of the *Akap6* DNA and RNA in living myoblasts and myocytes. Scale bar, 2 μm. **c** Bar graph showing the intensity sums for the *Akap6* RNA in myoblasts and myocytes. **d** Schematic showing the experimental design for visualizing the *Myog* DNA and RNA in primary myoblasts isolated from *Pax7*-Cre; SiCLAT mice and induced to undergo differentiation. **e** Representative images showing the visualization of *Myog* DNA and RNA in living myoblasts and myocytes. Scale bar, 2 μm. **f** Bar graph showing the intensity sum for the *Myog* RNA in myoblasts and myocytes

expression pattern of *Myog* measured by RNA-seq [24]. The exact co-localization of the *Myog* DNA and RNA signals indicated that SiCLAT showed good specificity in simultaneously labeling non-repetitive DNA and RNA (Fig. 5e). Additionally, we compared the RNA signal resistance to quenching in myocytes with that in fibroblasts

(negative control). The fibroblasts exhibited a very low channel intensity for the RNA signal, further confirming the specificity of *Myog* RNA imaging (Additional file 1: Fig. S14h, i, Fig.S15b-d). These results emphasize that SiCLAT offers a convenient and viable technological option for the in situ tracking of endogenous gene transcription, which enables co-imaging of gene loci and their transcripts.

SiCLAT enables visualization of chromatin loops and associated gene transcription

Lastly, we leveraged the SiCLAT live-cell imaging platform to test the ability of simultaneous labeling chromatin loop formation and associated transcriptional activity within a biological system. To test this, we conducted simultaneous visualization of the *Myog-Mybph* chromatin loop and its associated *Myog* gene transcription in living myocytes, with fibroblasts serving as a negative control. We successfully labeled the chromatin loop

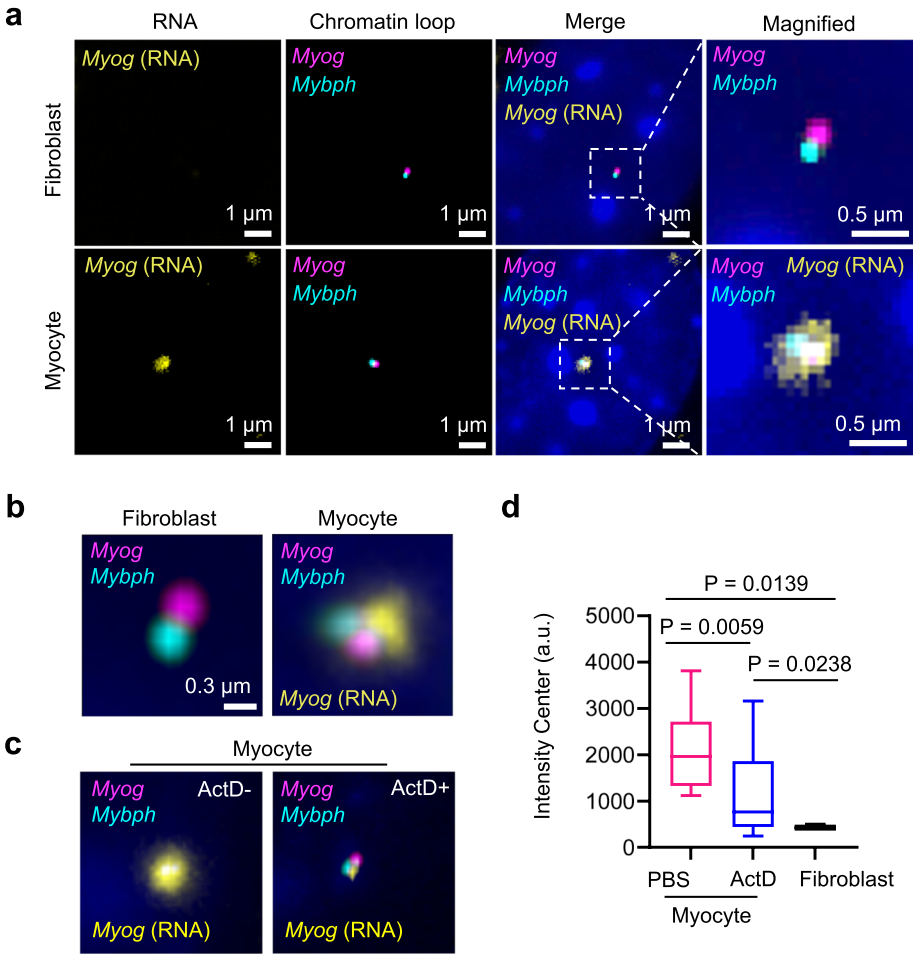

Fig. 6 SiCLAT enables visualization of a chromatin loop and associated gene transcription. **a** Representative images showing visualization of the *Myog-Mybph* chromatin loop and *Myog* RNA in living fibroblasts and myocytes. Scale bar, 1 μm (left), 0.5 μm (right). **b** Representative magnified snapshot images showing visualization of the *Myog-Mybph* chromatin loop and *Myog* RNA in living fibroblasts and myocytes. Scale bar, 0.3 μm. **c** Representative magnified snapshot images showing visualization of the *Myog-Mybph* chromatin loop and *Myog* RNA in living myocytes treated with ActD or PBS. **d** The center intensity of the *Myog* RNA in myoblasts treated with ActD or PBS. Fibroblasts served as a negative control

anchors in both cell types, whereas the *Myog* RNA was exclusively detected in myocytes (Fig. 6a), consistent with our above-described findings (Fig. 5e, f). We also quantified the RNA signal intensity in myocytes treated with Actinomycin D (ActD), an inhibitor of RNA polymerase elongation. The *Myog* RNA signal intensity was significantly weakened in ActD-treated myocytes (Fig. 6b–d), further validating the specificity of SiCLAT-mediated RNA imaging. In summary, our results reveal that the SiCLAT system provides a viable technological option for the direct observation of chromatin loop formation and its influence on transcriptional activation in living cells.

Discussion

The existing methods for DNA and RNA imaging rely heavily on engineered stable cell lines with manipulated genomic sequences, which limits our ability to understand chromatin dynamics and gene transcription across cell lineages. In this study, we developed a multifunctional transgenic mouse model, known as SiCLAT, to overcome these limitations. By introducing a dCas9-dCas13d cassette into the mouse genome, we achieved the co-expression of dCas9 and dCas13 proteins in cells from SiCLAT mice; this enabled the nuclear assembly of functional fluorescent ribonucleoproteins (fRNPs). Our innovative approach enables the simultaneous labeling of chromatin loops (non-repetitive DNA) and their associated gene transcription (RNA) in various cell types.

Over the past decade, researchers have used numerous technologies to investigate chromatin structure and function, and their findings have provided valuable insights into the spatial arrangement of the genome and alterations related to biological processes, such as differentiation [9, 24, 28, 29], cell cycle [30], and the G1 [8, 9, 15, 18], most of which have been assessed across timeframes of tens of minutes. These investigations have revealed that substantial alterations in chromatin organization occur during such processes, highlighting the critical role of imaging technologies in improving our understanding of the 4D genome [31, 32].

Although some editing- and DNA-FISH-based imaging methods have been reported for visualizing chromatin structures, such as CRISPR-tag, TriTag, and Tn5-FISH [9, 15, 16, 33–39], these methods limit their application in investigating functional E-P interaction in its native genomic environment. Moreover, solely labeling DNA in fixed cells could not simultaneously image RNA in the same cells is another weakness to elucidate how the dynamic E-P interaction regulates transcription in living cells during cell fate determination.

Recent reports have highlighted the dynamic and cell lineage-specific nature of enhancer-promoter (E-P) interactions and their regulatory effects on gene expression during development [8, 9, 24, 40, 41]. However, the underlying mechanisms through which dynamic *cis*-element interactions regulate gene expression remained largely unknown. The methods used to label RNA and between-gene differences in transcriptional speed can greatly affect the interpretation of data and lead to misjudgments about E-P and/or P-P interactions. These technical limitations of the current imaging systems have hindered investigations into dynamic E-P interactions and their roles in regulating gene transcription within living cells. Therefore, a method for live-cell simultaneous co-imaging of non-repetitive DNA and RNA is needed to help decipher the molecular mechanisms underlying dynamic E-P interactions and their functions in regulating

cell lineage-specific gene expression during normal development and under disease conditions.

Currently, two proposed models for E-P interaction: the structural bridge model and hub model [42–45]. In the structural bridge model, enhancer and promoter DNA are physically connected by a bridge formed by highly ordered protein–protein interactions [46, 47]. However, in the hub model, the effective E-P communication does not necessarily rely on enduring protein–protein interactions spanning the distance between enhancer and promoter DNA sequences. Instead, the emphasis is on localized concentrations of transcription-associated proteins. These proteins are drawn in by both the enhancer and promoter DNA, creating a local hub that facilitates bursts of transcription. Although the two models have been proposed for a while and, recently, there has been a growing preference for the "hub" model [9, 48], imaging evidence is still lacking to validate those two models in living cells. As the complexity of 4D genome organization and function in transcriptional regulation is cell-type and/or loci specific manners, it is highly possible that these two models are co-existence in living cells and functionally regulate transcriptional activation of genes in different loci during development. Our SiCLAT might provide a convenient and viable technological option imaging system to corroborate these two models in various cell lineages and loci specific fashion within living cells.

Furthermore, by crossing the SiCLAT mice with other model mice (e.g., conditional gene SiCLAT knockouts), our approach could theoretically be extended to explore other key questions in 3D genomes such as phase separation [49, 50], stripes formation [51, 52], and chromatin loop formation which may be mediated by epigenetic modification [50, 53] and/or the structural implications of architectural protein like cohesion [54], CTCF [55], MyoD [24], and YY1 [56]. SiCLAT thus has the potential to be broadly applied in addressing general and/or cell lineage-specific functions of proteins that contribute to genomic structure and transcriptional regulation for cell fate determination during development [57].

One of the important advantages and significant applications of the SiCLAT system is able to concurrent tracking of DNA and RNA in various primary cells. However, the use of primary cells also introduces certain limitations in phototoxicity, especially for the primary muscle stem cells utilized in this study, which are light-sensitive cells with small nuclei and do not attach flat like other "imaging model cells" such as U2OS and COS-7. In addition, we also found that other primary cells are more tolerant to phototoxicity than muscle stem cells, for example, fibroblast cells have good photosensitivity, which can resist multi-channel, multi-frame and Z-stack scanning in long-term imaging. Another limitation is the efficiency of labeling, which is more based on the percentage of the delivering fgRNA pool into the nucleus, which would be a difference in the efficiency of alleles labeling between the single cells even between the different primary cells. Some primary cells such as fibroblasts can absorb more fgRNA pool and have a higher labeling efficiency. Therefore, future efforts to overcome these limitations and advance new imaging technologies should focus on optimizing gRNA design and efficiency, developing improved strategies for directly targeting DNA, and enhancing the precision and continuity of imaging data using superior dyes. With such advancements, SiCLAT holds the potential to become an excellent imaging platform for in vivo DNA

and RNA tracking, potentially in combination with techniques such as tissue clearing [58]. Our new method offers unique advantages and is expected to be a powerful tool for exploring the 4D genome in future in vivo studies.

Conclusions

In summary, we present a convenient real-time imaging SiCLAT system to label the chromatin loop anchor interactions and associated gene transcription in living primary cells, which provides a reliable imaging tool for investigating the functional roles of the dynamic genome structure in regulating transcription activation within living cells.

Methods

Mouse lines and animal care

SiCLAT (CAG-LSL-dCas9-P2A-dCas13d-polyA) transgenic mice in the C57BL/6j background were generated by the Model Animal Research Center of Nanjing University. Mice were housed in a pathogen-free facility and given free access to water and standard rodent chow under the following conditions: 21 °C ambient temperature, 50–60% humidity, and 12 h dark/light cycle. All animal procedures were approved by the Animal Ethics Committee of Peking Union Medical College, Beijing, China (ACUC-A01-2016–003).

Primary myoblasts isolation, culture, and differentiation

Primary myoblasts were isolated from the hind-limb skeletal muscles of 2- to 3-week-old *Pax7*-Cre; SiCLAT or SiCLAT mice. The collected muscles were minced and digested in a mixture of type II collagenase and dispase. Cells were filtered from debris and centrifuged, and two rounds of differential attachment for 10 min per round were used to separate fibroblasts (attached) and myoblasts (non-attached). The myoblasts were cultured in growth medium (F-10 Ham's medium supplemented with 20% fetal bovine serum, 10 ng/ml basic fibroblast growth factor, 1% penicillin–streptomycin) on collagen-coated cell culture plates at 37 °C in 5% CO_2. For the differentiation of primary myoblasts, cells were transferred to differentiation medium (DM) consisting of DMEM (Gibco, Cat. N: C11995500BT) supplemented with 2% horse serum (Hyclone, Cat. N: SH30074.03) and 1% penicillin–streptomycin. All cells were grown to 70–80% confluence before induction of differentiation.

Primary hepatocyte isolation and culture

Primary hepatocytes were isolated from 8-week-old SiCLAT mice. A midline laparotomy was performed under anesthesia and the inferior vena cava was identified. Retrograde perfusion of the liver was achieved via cannulation of the inferior vena cava. The hepatic portal vein was transected to allow the perfusate to flow out. The liver was sequentially perfused with the following solutions (flow rate, 5 ml/min; constant-flow pump, BT100-02, Qili): 60 ml of Hank's balanced salt solution (HBSS, Gibco, 14190136) with 0.5 mM EDTA (Sigma-Aldrich); 1 M glucose, 1% penicillin–streptomycin; and 50 ml of HBSS plus 5 mM $CaCl_2$ (Sigma-Aldrich), 1 mg/mL of collagenase type IV (Gibco), 1 M glucose, and 1% penicillin–streptomycin. All solutions were warmed to 37 °C. The gall bladder was removed and discarded. Liver lobes were carefully collected to avoid damage,

transferred to a Petri dish containing DMEM with 10% FBS, and gently agitated to disperse the hepatocytes. The hepatocyte slurry was transferred to a 50-ml conical tube and washed with DMEM containing 10% FBS by centrifugation at 50 g for 5 min. The hepatocyte pellet was gently resuspended in 15 ml PBS at room temperature and then mixed with 9 ml of Percoll (Solarbio, P8370). The mixture was centrifuged at 50 g for 15 min at room temperature. Debris and excess solution were aspirated and the hepatocyte pellet washed twice as described above. Viable hepatocytes were resuspended in DMEM containing 10% FBS and counted on a hemocytometer using Trypan Blue exclusion. The obtained cells were seeded in DMEM plating medium containing 10% FBS and 1% penicillin–streptomycin.

Primary neural stem cell isolation and culture

Primary neural stem cells (NSCs) were isolated from SiCLAT mouse embryos at embryonic days 14–16 (E14-16). Pregnant mice were euthanized and uteri were carefully removed. The fetal mouse skulls were dissected and the anterior cortex was gently separated and rinsed in 2–4 ml complete culture medium. The tissue was gently triturated, the obtained cell suspension was centrifuged at 1000 rpm, the cell pellet was resuspended with Accutase enzyme and incubated for 10–15 min, and the digested sample was filtered, centrifuged, resuspended, seeded in complete culture medium [DMEM/F12 supplemented with 2% B27 (Invitrogen), 1% penicillin–streptomycin (Invitrogen), 1% GlutaMAX (Invitrogen), and 20 ng/mL each of bFGF and EGF (PeproTech, USA)], and incubated at 37 °C in 5% CO_2.

Primary kidney cell isolation and culture

Briefly, mouse kidneys were collected and dissected, the renal cortex was diced and digested with collagenase (0.5 mg/mL), and the reaction was terminated with fetal bovine serum (FBS). Gravity sedimentation was performed, and glomeruli and other remaining tissue clumps were decanted from the sedimented tubules. The retained sample was washed twice with medium and the tubules were resuspended in tubular cell culture medium (DMEM with FBS). The tubule epithelial cells were cultured for 4 to 5 days before being used for experiments.

Primary preadipocyte isolation and culture

Stromal vascular fraction (SVF) cells were isolated from the iWAT of 3- to 4-week-old SiCLAT mice and cultured in DMEM/F-12 (GIBCO) supplemented with 10% neonatal calf serum (NCS, Capricorn Scientific) in 5% CO_2 at 37 °C.

Transfection and electroporation

Primary cells isolated from *Pax7*-Cre; SiCLAT or SiCLAT mice were seeded to 60-mm dishes. Cells were transfected with 5 μg plasmid expressing dCas9-EGFP using jetOPTIMUS®. The dCas9-EGFP (Addgene 51023) plasmid was gifted by Antony K. Chen from Peking University. The fluorescent gRNA pools were annealed and electroporated into the various primary cells (about 1×10^6) using a 4D-Nucleofector™ X Unit (Lonza, Catalog#: V4XC-1024) running programs CD-137 or CD-112. The electroporated cells were

plated on collagen-coated Nunc Glass Bottom Dishes (Thermo Fisher, 150680) and cultured for 12–24 h prior to imaging.

gRNA synthesis and annealing

For labeling of repetitive and non-repetitive sequences, the crRNAs were synthesized by IDT or Sango and 3′-end modified with a chemical fluorophore (Atto647N, Atto488, FAM, TAMRA, Cy5). The full-length tracrRNA was non-fluorescently synthesized by IDT (Integrated DNA Technologies, Redwood City, CA) or Sango. The fluorescent crRNAs were annealed with tracrRNA at an equal molar ratio in folding buffer (20 mM HEPES, pH 7.5, and 150 mM KCl), incubated at 95 °C for 5 min, incubated at 70 °C for 5 min, gradually cooled to room temperature, supplemented with 1 mM $MgCl_2$, incubated at 40 °C for 5 min, and gradually cooled to room temperature [22]. The sequences of the utilized tracrRNA and crRNAs are presented in Additional file 8: Table S1-2.

Live-cell imaging

Before image acquisition, the equipment and objective were allowed to equilibrate to 37 °C for about 1 h. Primary living cells were grown for 24 h in a collagen-coated 35-mm glass-bottom dish (Nunc). The medium was changed to phenol red-free DMEM before imaging. The cells were equilibrated in a humidified incubation chamber (37 °C, 5% CO_2) for 1 h and loaded to a Leica TCS SP8 STED microscope or Dragonfly200. The Leica microscope was equipped with the spectral flexibility of WLL for excitation, HC PL 63 × /1.4 oil and HC PL APO 100 × /1.4 oil objective with immersion oil based on the DMi8 Inverted Microscope equipped, and sCMOS camera in the wide-field imaging and HyD detector in the confocal imaging.

Non-repetitive sequence imaging was acquired using the following parameters for confocal microscopy: pixel size, X: 114 nm, Y: 114 nm, Z: 297 nm; for wide-field microscopy: pixel size, X: 103 nm, Y: 103 nm, Z: 213 nm. Imaging was performed using maximum intensity projection with Z stacks from 0.24 to 12 μm (step: 0.24–0.26 μm) after deconvolution. Optimal image processing was performed with lighting on a Leica TCS SP8 STED. All imaging data shown to calculate 3D distances or fluorescence intensities were performed max intensity projection.

Super-resolution imaging

The labeling signal was captured in Multi-SIM (multimodality structured illumination microscopy) with 3D-SIM model in the living cell. SIM images were acquired on a Multi-SIM imaging system (NanoInsights-Tech Co., Ltd.) equipped with a 100 × 1.49NA oil objective (Nikon CFI SR HP Apo) and sCMOS (complementary metal–oxide–semiconductor) camera (Kinetix, Teledyne Imaging). Images were acquired by VSIM software and then reconstructed using the SIM Imaging Analyser software (NanoInsights-Tech). During image acquisition, cells are in a humidified chamber maintained at 37 °C in the presence of 5% CO_2.

Tn5-FISH

Tn5-FISH was performed according to a previously reported (Tn5-FISH) [33]. Briefly, the probe library was generated by PCR amplification and recovered using a DNA

Cleanup kit (TIANGEN, Cat.N: DP203-02). After recovering using the DNA Cleanup kit, salmon sperm DNA (Invitrogen, Cat.N: 18,440,016) was added into the Tn5-FISH probes (50 mg of salmon sperm DNA per 1 mg of Tn5-FISH probes), ethanol precipitated, and dissolved in DNA FISH buffer, 50% deionized formamide (Ambion, Cat.N: AM9342), 10% dextran sulfate (VWR, Cat.N: 9011–18-1), 2 × SSC (Invitrogen, Cat.N: 15557044), at a concentration of 20 ng/ul of Tn5-FISH probes. The Tn5-FISH probes were amplified by a second PCR with fluorescence-tagged primers. The in situ hybridization procedure of Tn5-FISH was similar to that of traditional FISH, as previously described [59]. Microscopic imaging was performed on a Leica TCS SP8 STED equipped with the spectral flexibility of white-light laser (WLL) for excitation and an HC PL APO × 100/1.4 oil or objective. The sequences of the utilized primer are presented in Additional file 8: Table S3.

Real-time RT-PCR analyses

Total RNA was extracted from cells with TRIZOL reagent and reverse-transcribed (RT) using RevertAid reverse transcriptase (Thermo Scientific, EP0442). For measuring mature MyoG, quantitative PCR (qPCR) analyses were performed with the Soso-Fast qPCR Master Mix (Bio-Rad, 1,725,202) using an iQ5 Multicolor Real-Time PCR Detection System (Bio-Rad). GAPDH served as an internal control. All primers used for RT-qPCR are listed in Additional file 8: Table S4.

Correction for chromatic aberration

To correct for chromatic aberrations, we imaged 100-nm TetraSpeck Microspheres (T7279, Invitrogen). The microspheres were diluted, mixed with imaging medium, and detected using the same equipment and imaging parameters applied in our study. The detected chromatic aberrations were corrected by aligning and adjusting the equipment.

Deconvolution

From the 4D images, single-cell regions were cropped on the X Y Z or X Y Z T axes. The imaging data were exported from the microscope software in “lif file “ format. Deconvolution was performed using the Huygens software with wizard function. The following imaging parameters were adjusted: channel (excitation and emission wavelengths), type of microscope, material of vehicle, imaging optical path media, automatically generated theoretical PSF, Measure PSF, Crop the image (optional), Select Channel, estimating parameters, set the Background value, select the deconvolution algorithm, adjust the deconvolution setup on Maximum iterations, signal-to-noise ratio (SNR), Quality threshold, iteration mode, bleaching correction, brick layout, Evaluate effects and proceed to the next channel, correct the Z-drift based nucleus and Done the deconvolution process. After deconvolution and correction of chromatic aberration were performed using the Huygens software, an”ICS2 file “ was generated and used for calculations.

Spot generation

The ICS2 outputs were loaded in the Imaris software for Imaris-based spot generation. Each spot stores information on the position (X, Y, Z), diameter (X, Y, Z), and time point. The specific position of each spot in the live-cell imaging data was positioned based on

the Imaris spot function with 3D Gaussian fitting using each fluorescence channel's maximum values corresponding to the different channels in every cropped image. The 3D rectangular boundary was set based on the image size. The spots formed as a vector ($\overrightarrow{p}$) based on the 3D coordinates of the rectangular boundary to calculate the 3D distance between the different spots, as follows:

$$\overrightarrow{p} = \left[p_x, p_y, p_z\right].$$

Distance measurement

The 3D distances between different spots were calculated using the function module "spot displacement X, Y, Z" in the Imaris software. The displacement $\overrightarrow{d}(t)$ reflected the distance that a spot moved between two sequential time points. It was calculated for each axis by subtracting the last time point position $\overrightarrow{p}(t-1)$ from the selected time point position $\overrightarrow{p}(t)$, as follows:

$$\overrightarrow{d}(t) = \overrightarrow{p}(t) - \overrightarrow{p}(t-1).$$

The area of E1, E3, and P in the Actc1 multi-locus interaction calculated with Heron's formula as follows:

$$S = \sqrt{p(p-a)(p-b)(p-c)}p = \frac{a+b+c}{2}$$

S stands for the area; a, b, c stands for the length of the three chromatin loop anchors distance; p stands for the semi-perimeter.

RNA intensity calculation

The RNA intensity in living cells was calculated from the raw data using the "Spots" function of Imaris, which estimated the 1.00-μm XY diameter and 1.50-μm Z diameter (model PSF: elongation along *Z*-axis). The RNA intensity was estimated, the output intensity was summed, and the intensity center was calculated. The background intensity was used to calculate the relative fluorescence intensity. No deconvolution was applied to the RNA intensity calculations.

Visualization of specific DNA and RNA sequences

To visualize the *Akap6* DNA and RNA in the various primary cells, crRNAs were designed to target the *Akap6* DNA and RNA sequences based on repeats. To label the repetitive sequences, the crRNA was annealed with tracrRNA to 50–100 pmol and delivered into 1×10^6–1×10^7 primary cells, with the utilized number determined based on the electroporation efficiency. To label non-repetitive sequences, each crRNA was applied at 20–30 pmol. The transfected cells were plated on collagen-coated 35-mm glass-bottom dishes (Nunc) and cultured for 12–24 h before imaging. For *Akap6* and *Myog* DNA and RNA imaging in myocytes, transfected myoblasts were plated and differentiation was induced by switching attached cells to differentiation medium (DM). Nuclei were visualized using DAPI for fixed cells and NucBlue™ Live ReadyProbes™ (Thermo Fisher, R37605) for living cells.

Visualization

Tracks of Hi-C maps, ATAC-seq, and ChIP-seq data were generated by Juicebox. The Hi-C data and ChIP-seq were analyzed as our previously reported [24, 27]. JuicerBox v.2.17.00 [60] was used to generate the Hi-C heatmap and manual correction. The KR-normalized method was applied for the visualization of Hi-C data [61].

Western blot analysis

Primary cells were lysed in RIPA lysis buffer. Proteins in lysates were resolved by SDS-PAGE and transferred to a polyvinylidene difluoride membrane. Immunoblotting was performed using primary antibodies against. Protein lysates were resolved by SDS-PAGE, transferred to a polyvinylidene fluoride (PVDF) membrane, and immunoblotted with primary antibodies against MyoD (Santa Cruz, sc32758, 1:500) and β-tubulin (CMCTAG, AT0003, 1:1000).

Statistical analysis

All data are shown as means ± SD of at least three replicates. Statistical analyses were applied using the GraphPad Prism software (San Diego, CA, USA, version 9.3.1). Two-tailed Student's *t*-test was used to determine the *p* value between two groups; ns indicates not significant.

Supplementary Information

The online version contains supplementary material available at https://doi.org/10.1186/s13059-024-03463-9.

Additional file 1: Fig. S1-S15.

Additional file 2: Video S1. Three-dimensional section view of the 3D *Myog* and *Mybph* non-repetitive DNA sequence imaging in myoblast. *Myog* anchor: red, *Mybph* anchor: green.

Additional file 3: Video S2. Three-dimensional rotation view of the 3D *Myog* and *Mybph* non-repetitive DNA sequence imaging in myoblast. *Myog* anchor: red, *Mybph* anchor: green.

Additional file 4: Video S3. Three-dimensional section view of the *Actc1* multi-locus interaction imaging in the myoblast. *Actc1-Promoter*: blue, *Actc1-Enhancer1*: yellow, *Actc1-enhancer3*: purple.

Additional file 5: Video S4. Three-dimensional rotation view of the 3D *Actc1* multi-locus interaction imaging in the myoblast. *Actc1-Promoter*: blue, *Actc1-Enhancer1*: yellow, *Actc1-enhancer3*: purple.

Additional file 6: Video S5. Labeling *Myog-Mybph* chromatin loop in the living myoblast and myocyte at intervals of 30 seconds, capturing data over 10 minutes. The *Myog-Mybph* chromatin loop distance was calculated and shown at every point in time.

Additional file 7: Video S6. The Akap6 DNA and RNA imaging in the myoblast induced differentiation for 60 minutes. The relative intensity of *Akap6* DNA and RNA was calculated and shown at every point in time.

Additional file 8: Table S1: The fgRNA sequence for repetitive DNA and RNA visualization. Table S2: The fgRNA sequence for non-repetitive DNA and RNA visualization. Table S3: Primers using for Tn5-FISH. Table S4: Primers using for RT-qPCR.

Additional file 9. Review history.

Acknowledgements
Not applicable.

Peer review information
Andrew Cosgrove was the primary editor of this article and managed its editorial process and peer review in collaboration with the rest of the editorial team.

Review history
The review history is available as Additional file 9.

Authors' contributions
D.Z., and Y.Z. supervised the project. Y.Z., and X.W. designed the model. X.W. performed all imaging experiments. J.K., and L.L. contributed to support and technical guidance of the imaging platform. Y.Y., and F.C. performed all computational and bioinformatics analysis. X.H., and G.L. helped to isolate the primary cell. X.N. helped to mouse breeding. D.Z., and H.L. helped to design experiments. X.W., D.Z., and Y.Z. wrote the manuscript.

Funding
This work was supported by grants from the National Key R&D Program of China (2021YFA1100202, 2022YFA0806002), the National Natural Science Foundation of China (31971080, 91949106), the Basic Research Projects of Basic Strengthening Program (2020-JCJQ-ZD-264), and the CAMS Innovation Fund for Medical Sciences (2021- I2M-1–019).

Data availability
All data generated or analyzed during this study are included in this published article and its supplementary information files. All microscopy data and uncropped western blot data are available in Figshare [62].

Declarations

Ethics approval and consent to participate
All animal procedures were approved by the Animal Ethics Committee of Peking Union Medical College, Beijing, China (ACUC-A01-2016–003).

Competing interests
The authors declare no competing interests.

Received: 19 October 2023 Accepted: 17 December 2024
Published online: 02 January 2025

References

1. Lieberman-Aiden E, van Berkum NL, Williams L, Imakaev M, Ragoczy T, Telling A, Amit I, Lajoie BR, Sabo PJ, Dorschner MO, et al. Comprehensive mapping of long-range interactions reveals folding principles of the human genome. Science. 2009;326:289–93.
2. Rao SS, Huntley MH, Durand NC, Stamenova EK, Bochkov ID, Robinson JT, Sanborn AL, Machol I, Omer AD, Lander ES, Aiden EL. A 3D map of the human genome at kilobase resolution reveals principles of chromatin looping. Cell. 2014;159:1665–80.
3. Mateo LJ, Murphy SE, Hafner A, Cinquini IS, Walker CA, Boettiger AN. Visualizing DNA folding and RNA in embryos at single-cell resolution. Nature. 2019;568:49–54.
4. Su JH, Zheng P, Kinrot SS, Bintu B, Zhuang X. Genome-scale imaging of the 3D organization and transcriptional activity of chromatin. Cell. 2020;182:1641-1659 e1626.
5. Liu M, Lu Y, Yang B, Chen Y, Radda JSD, Hu M, Katz SG, Wang S. Multiplexed imaging of nucleome architectures in single cells of mammalian tissue. Nat Commun. 2020;11:2907.
6. Cardozo Gizzi AM, Cattoni DI, Fiche J-B, Espinola SM, Gurgo J, Messina O, Houbron C, Ogiyama Y, Papadopoulos GL, Cavalli G, et al. Microscopy-based chromosome conformation capture enables simultaneous visualization of genome organization and transcription in intact organisms. Mol Cell. 2019;74:212-222.e215.
7. Espinola SM, Götz M, Bellec M, Messina O, Fiche JB, Houbron C, Dejean M, Reim I, Cardozo Gizzi AM, Lagha M, Nollmann M. Cis-regulatory chromatin loops arise before TADs and gene activation, and are independent of cell fate during early Drosophila development. Nat Genet. 2021;53:477–86.
8. Chen H, Levo M, Barinov L, Fujioka M, Jaynes JB, Gregor T. Dynamic interplay between enhancer-promoter topology and gene activity. Nat Genet. 2018;50:1296–303.
9. Alexander JM, Guan J, Li B, Maliskova L, Song M, Shen Y, Huang B, Lomvardas S, Weiner OD. Live-cell imaging reveals enhancer-dependent Sox2 transcription in the absence of enhancer proximity. Elife. 2019;8:e41769.
10. Ong C-T, Corces VG. Enhancer function: new insights into the regulation of tissue-specific gene expression. Nat Rev Genet. 2011;12:283–93.
11. Andersson R, Gebhard C, Miguel-Escalada I, Hoof I, Bornholdt J, Boyd M, Chen Y, Zhao X, Schmidl C, Suzuki T, et al. An atlas of active enhancers across human cell types and tissues. Nature. 2014;507:455–61.
12. Bergman DT, Jones TR, Liu V, Ray J, Jagoda E, Siraj L, Kang HY, Nasser J, Kane M, Rios A, et al. Compatibility rules of human enhancer and promoter sequences. Nature. 2022;607:176–84.
13. Galouzis CC, Furlong EEM. Regulating specificity in enhancer-promoter communication. Curr Opin Cell Biol. 2022;75:102065.
14. Chen Z, Snetkova V, Bower G, Jacinto S, Clock B, Dizehchi A, Barozzi I, Mannion BJ, Alcaina-Caro A, Lopez-Rios J, et al. Increased enhancer–promoter interactions during developmental enhancer activation in mammals. Nat Genet. 2024;56:675–85.
15. Gabriele M, Brandao HB, Grosse-Holz S, Jha A, Dailey GM, Cattoglio C, Hsieh TS, Mirny L, Zechner C, Hansen AS. Dynamics of CTCF- and cohesin-mediated chromatin looping revealed by live-cell imaging. Science. 2022;376:496–501.
16. Chen B, Zou W, Xu H, Liang Y, Huang B. Efficient labeling and imaging of protein-coding genes in living cells using CRISPR-Tag. Nat Commun. 2018;9:5065.
17. Xu H, Wang J, Liang Y, Fu Y, Li S, Huang J, Xu H, Zou W, Chen B. TriTag: an integrative tool to correlate chromatin dynamics and gene expression in living cells. Nucleic Acids Res. 2020;48:e127.

18. Clow PA, Du M, Jillette N, Taghbalout A, Zhu JJ, Cheng AW. CRISPR-mediated multiplexed live cell imaging of nonrepetitive genomic loci with one guide RNA per locus. Nat Commun. 1871;2022:13.
19. Lyu XY, Deng Y, Huang XY, Li ZZ, Fang GQ, Yang D, Wang FL, Kang W, Shen EZ, Song CQ. CRISPR FISHer enables high-sensitivity imaging of nonrepetitive DNA in living cells through phase separation-mediated signal amplification. Cell Res. 2022;32:969–81.
20. Peng Q, Huang Z, Sun K, Liu Y, Yoon CW, Harrison RES, Schmitt DL, Zhu L, Wu Y, Tasan I, et al. Engineering inducible biomolecular assemblies for genome imaging and manipulation in living cells. Nat Commun. 2022;13:7933.
21. Fu Y, Rocha PP, Luo VM, Raviram R, Deng Y, Mazzoni EO, Skok JA. CRISPR-dCas9 and sgRNA scaffolds enable dual-colour live imaging of satellite sequences and repeat-enriched individual loci. Nat Commun. 2016;7:11707.
22. Wang H, Nakamura M, Abbott TR, Zhao D, Luo K, Yu C, Nguyen CM, Lo A, Daley TP, La Russa M, et al. CRISPR-mediated live imaging of genome editing and transcription. Science. 2019;365:1301–5.
23. Chen B, Gilbert LA, Cimini BA, Schnitzbauer J, Zhang W, Li GW, Park J, Blackburn EH, Weissman JS, Qi LS, Huang B. Dynamic imaging of genomic loci in living human cells by an optimized CRISPR/Cas system. Cell. 2013;155:1479–91.
24. Wang R, Chen F, Chen Q, Wan X, Shi M, Chen AK, Ma Z, Li G, Wang M, Ying Y, et al. MyoD is a 3D genome structure organizer for muscle cell identity. Nat Commun. 2022;13:205.
25. Sanyal A, Lajoie BR, Jain G, Dekker J. The long-range interaction landscape of gene promoters. Nature. 2012;489:109–13.
26. Jin F, Li Y, Dixon JR, Selvaraj S, Ye Z, Lee AY, Yen CA, Schmitt AD, Espinoza CA, Ren B. A high-resolution map of the three-dimensional chromatin interactome in human cells. Nature. 2013;503:290–4.
27. Liu Y, Wan X, Li H, Chen Y, Hu X, Chen H, Zhu D, Li C, Zhang Y. CTCF coordinates cell fate specification via orchestrating regulatory hubs with pioneer transcription factors. Cell Rep. 2023;42:113259.
28. Gu B, Swigut T, Spencley A, Bauer MR, Chung M, Meyer T, Wysocka J. Transcription-coupled changes in nuclear mobility of mammalian cis-regulatory elements. Science. 2018;359:1050–5.
29. Linares-Saldana R, Kim W, Bolar NA, Zhang H, Koch-Bojalad BA, Yoon S, Shah PP, Karnay A, Park DS, Luppino JM, et al. BRD4 orchestrates genome folding to promote neural crest differentiation. Nat Genet. 2021;53:1480–92.
30. Zhang H, Emerson DJ, Gilgenast TG, Titus KR, Lan Y, Huang P, Zhang D, Wang H, Keller CA, Giardine B, et al. Chromatin structure dynamics during the mitosis-to-G1 phase transition. Nature. 2019;576:158–62.
31. Cosma MP, Neguembor MV. The magic of unraveling genome architecture and function. Cell Rep. 2023;42:112361.
32. Dekker J, Alber F, Aufmkolk S, Beliveau BJ, Bruneau BG, Belmont AS, Bintu L, Boettiger A, Calandrelli R, Disteche CM, et al. Spatial and temporal organization of the genome: current state and future aims of the 4D nucleome project. Mol Cell. 2023;83:2624–40.
33. Niu J, Zhang X, Li G, Yan P, Yan Q, Dai Q, Jin D, Shen X, Wang J, Zhang MQ, Gao J. A novel cytogenetic method to image chromatin interactions at subkilobase resolution: Tn5 transposase-based fluorescence in situ hybridization. J Genet Genomics. 2020;47:727–35.
34. Beliveau BJ, Kishi JY, Nir G, Sasaki HM, Saka SK, Nguyen SC, Wu CT, Yin P. OligoMiner provides a rapid, flexible environment for the design of genome-scale oligonucleotide in situ hybridization probes. Proc Natl Acad Sci U S A. 2018;115:E2183–92.
35. Moffitt JR, Hao J, Wang G, Chen KH, Babcock HP, Zhuang X. High-throughput single-cell gene-expression profiling with multiplexed error-robust fluorescence in situ hybridization. Proc Natl Acad Sci U S A. 2016;113:11046–51.
36. Chen KH, Boettiger AN, Moffitt JR, Wang S, Zhuang X. RNA imaging. Spatially resolved, highly multiplexed RNA profiling in single cells. Science. 2015;348:aaa6090.
37. Bienko M, Crosetto N, Teytelman L, Klemm S, Itzkovitz S, van Oudenaarden A. A versatile genome-scale PCR-based pipeline for high-definition DNA FISH. Nat Methods. 2013;10:122–4.
38. Beliveau BJ, Joyce EF, Apostolopoulos N, Yilmaz F, Fonseka CY, McCole RB, Chang Y, Li JB, Senaratne TN, Williams BR, et al. Versatile design and synthesis platform for visualizing genomes with Oligopaint FISH probes. Proc Natl Acad Sci U S A. 2012;109:21301–6.
39. Cremer M, Grasser F, Lanctot C, Muller S, Neusser M, Zinner R, Solovei I, Cremer T. Multicolor 3D fluorescence in situ hybridization for imaging interphase chromosomes. Methods Mol Biol. 2008;463:205–39.
40. Zuin J, Roth G, Zhan Y, Cramard J, Redolfi J, Piskadlo E, Mach P, Kryzhanovska M, Tihanyi G, Kohler H, et al. Nonlinear control of transcription through enhancer-promoter interactions. Nature. 2022;604:571–7.
41. Li J, Hsu A, Hua Y, Wang G, Cheng L, Ochiai H, Yamamoto T, Pertsinidis A. Single-gene imaging links genome topology, promoter-enhancer communication and transcription control. Nat Struct Mol Biol. 2020;27:1032–40.
42. Barshad G, Lewis JJ, Chivu AG, Abuhashem A, Krietenstein N, Rice EJ, Ma Y, Wang Z, Rando OJ, Hadjantonakis AK, Danko CG. RNA polymerase II dynamics shape enhancer-promoter interactions. Nat Genet. 2023;55:1370–80.
43. Lim B, Levine MS. Enhancer-promoter communication: hubs or loops? Curr Opin Genet Dev. 2021;67:5–9.
44. Hamamoto K, Fukaya T. Molecular architecture of enhancer-promoter interaction. Curr Opin Cell Biol. 2022;74:62–70.
45. Di Giammartino DC, Polyzos A, Apostolou E. Transcription factors: building hubs in the 3D space. Cell Cycle. 2020;19:2395–410.
46. Schoenfelder S, Fraser P. Long-range enhancer-promoter contacts in gene expression control. Nat Rev Genet. 2019;20:437–55.
47. Robson MI, Ringel AR, Mundlos S. Regulatory landscaping: how enhancer-promoter communication is sculpted in 3D. Mol Cell. 2019;74:1110–22.
48. Benabdallah NS, Williamson I, Illingworth RS, Kane L, Boyle S, Sengupta D, Grimes GR, Therizols P, Bickmore WA. Decreased enhancer-promoter proximity accompanying enhancer activation. Mol Cell. 2019;76:473-484 e477.
49. Wei C, Jia L, Huang X, Tan J, Wang M, Niu J, Hou Y, Sun J, Zeng P, Wang J, et al. CTCF organizes inter-A compartment interactions through RYBP-dependent phase separation. Cell Res. 2022;32:744–60.
50. Hsieh THS, Cattoglio C, Slobodyanyuk E, Hansen AS, Darzacq X, Tjian R. Enhancer-promoter interactions and transcription are largely maintained upon acute loss of CTCF, cohesin, WAPL or YY1. Nat Genet. 2022;54:1919–32.
51. Vian L, Pękowska A, Rao SSP, Kieffer-Kwon K-R, Jung S, Baranello L, Huang S-C, El Khattabi L, Dose M, Pruett N, et al. The energetics and physiological impact of cohesin extrusion. Cell. 2018;173:1165-1178.e20.

52. Kraft K, Magg A, Heinrich V, Riemenschneider C, Schöpflin R, Markowski J, Ibrahim DM, Acuna-Hidalgo R, Despang A, Andrey G, et al. Serial genomic inversions induce tissue-specific architectural stripes, gene misexpression and congenital malformations. Nat Cell Biol. 2019;21:305–10.
53. Zenk F, Zhan Y, Kos P, Loser E, Atinbayeva N, Schachtle M, Tiana G, Giorgetti L, Iovino N. HP1 drives de novo 3D genome reorganization in early Drosophila embryos. Nature. 2021;593:289–93.
54. Rao SSP, Huang SC, St Glenn Hilaire B, Engreitz JM, Perez EM, Kieffer-Kwon KR, Sanborn AL, Johnstone SE, Bascom GD, Bochkov ID, et al. Cohesin loss eliminates all loop domains. Cell. 2017;171:305-320 e324.
55. Nora EP, Goloborodko A, Valton AL, Gibcus JH, Uebersohn A, Abdennur N, Dekker J, Mirny LA, Bruneau BG. Targeted degradation of CTCF decouples local insulation of chromosome domains from genomic compartmentalization. Cell. 2017;169:930-944 e922.
56. Weintraub AS, Li CH, Zamudio AV, Sigova AA, Hannett NM, Day DS, Abraham BJ, Cohen MA, Nabet B, Buckley DL, et al. YY1 is a structural regulator of enhancer-promoter loops. Cell. 2017;171:1573-1588 e1528.
57. Stadhouders R, Filion GJ, Graf T. Transcription factors and 3D genome conformation in cell-fate decisions. Nature. 2019;569:345–54.
58. Jing D, Zhang S, Luo W, Gao X, Men Y, Ma C, Liu X, Yi Y, Bugde A, Zhou BO, et al. Tissue clearing of both hard and soft tissue organs with the PEGASOS method. Cell Res. 2018;28:803–18.
59. Bayani J, Squire JA. Fluorescence in situ hybridization (FISH). Curr Protoc Cell Biol. 2004;23: 22.4.1-22.4.52. https://doi.org/10.1002/0471143030.cb2204s23.
60. Durand NC, Robinson JT, Shamim MS, Machol I, Mesirov JP, Lander ES, Aiden EL. Juicebox provides a visualization system for Hi-C contact maps with unlimited zoom. Cell Syst. 2016;3:99–101.
61. Knight PA, Ruiz D. A fast algorithm for matrix balancing. IMA J Numer Anal. 2013;33:1029–47.
62. Xin Wan, Jie Kong, Xiaodi Hu, Lulu Liu, Yuanping Yang, Hu Li, Gaoao Liu, Xingchen Niu, Fengling Chen, Dan Zhang, Dahai Zhu, Yong Zhang: SiCLAT: simultaneous imaging of chromatin loops and active transcription in living cells. Figshare. 2024. https://doi.org/10.6084/m9.figshare.27934926.

Publisher's Note